RESEARCH Revista Mexicana de Física **64** (2018) 381–391 JULY-AUGUST 2018

Effect of Re and Tm-site on morphology structure and optical band gap of $ReTm\mathrm{O}_3$(Re = La, Ce Nd, Gd, Dy, Y and Tm = Fe, Cr) prepared by sol-gel method

M. Tufiq Jamil[a,*], J. Ahmad[a], S. Hamad Bukhari[b], and M. Saleem[c]
[a] *Department of Physics, Bahauddin Zakariya University, Multan 60800, Pakistan.*
[b] *Department of Physics, G. C. University Faisalabad, Layyah Campus, Layyah 31200, Pakistan.*
[c] *Department of Physics, Syed Babar Ali School of Sciences and Engineering (SBASSE),*
Lahore University of Management Sciences (LUMS), Opposite Sector U, DHA, Lahore 54792, Pakistan.
[*] *e-mail: tufiqjamil@yahoo.com*

Received 22 January 2018; accepted 14 April 2018

Rare earth nano sized pollycrystalline orthoferrites and orthocromites $ReTm\mathrm{O}_3$ (Re = La, Nd, Gd, Dy, Y and Tm = Fe, Cr) have been synthesized by sol-gel auto combustion citrate method. The samples have been characterized by means of X-ray diffraction (XRD), scanning electron microscope (SEM), energy dispersive X-ray spectroscopy (EDX), and UV-visible spectroscopy. The samples are single phase, as confirmed by XRD analysis, and correspond to the orthorhombic crystal symmetry with space group *pbnm*. Debye Scherer formula and Williamson Hall analysis have been used to calculate the average grain size, which is consistent with that of determined from SEM analysis and varied between 25-75 nm. The elemental compositions of all samples have been checked by EDX analysis. Different crystallographic parameters are calculated with strong structural correlation among *Re* and *Tm* sites. The optical energy band gap has been calculated by using Tauc relation estimated to be in the range of 1.77 - 1.87 eV and 2.77 - 3.14 eV, for $Re\mathrm{FeO}_3$ and $Re\mathrm{CrO}_3$, respectively.

Keywords: Sol-gel method; orthoferrites and orthocromites; optical band gap; structural characteristics.

PACS: 61.05.cp; 73.63.Bd

1. Introduction

$ReTm\mathrm{O}_3$ perovskite-type oxides (with Re = rare earth and Tm = transition metal) are much promising materials because they exhibit strong interactions among the partially filled f-shells electrons or *d*-shells of *Re* and *Tm* ions with oxygen ions (O) giving many interesting properties such as colossal magnetoresistance, high temperature superconductivity, charge/orbital ordering, metal-insulator transition [1-3] and can also be used in recent technologies such as solid oxide fuel cell [4], catalysts [5], electrodes materials [6] and chemical sensors [7]. An interesting feature of $ReTm\mathrm{O}_3$ is related to the variation in *Re*-O and *Tm*-O interactions that can be observed by varying *Re* ionic size as well as distortions in $Tm\mathrm{O}_6$ octahedra due to variation in ionic radius of transition metal (*Tm*). The positions of ions in the unit cell of $ReTm\mathrm{O}_3$ are shown in Fig. 1. The rare earth manganites $Re\mathrm{MnO}_3$ exhibit semiconducting behavior at room temperature, as well as strong magnetoelectric coupling below Neel transition temperature (T_N). Different compounds of the $Re\mathrm{MnO}_3$ have been synthesized by sol-gel method resulting in remarkable physical properties [8–13]. Nanoparticles of rare earth cobaltate perovskite $Re\mathrm{CoO}_3$ were also synthesized by many researchers with sol-gel method and these compounds also exhibiting orthorhombic crystal symmetry with some interesting physical properties [14-18]. Synthesis of nano-scaled materials are getting much interest, since fine powder usually shows superior properties such as higher chemical reactivity, better sinterability and large surface area [19,20]. Recently, preparation and magnetic properties were discussed of perovskite $Re\mathrm{FeO}_3$ nanocrystalline powders by combustion of nitrate-citrate gel [21, 22], and magnetic and electrical properties of $Re\mathrm{CrO}_3$ synthesize by hydrothermal and sol-gel method [23, 24] highlighted the major role of synthesis technique on the physical properties of the compounds. However, there have been no reports on the comprehensive analysis of their structural correlation with respect to different *Re* and *Tm* sites. In this study, we focus on the morphology, structural and optical properties of $ReTm\mathrm{O}_3$ (Re = La, Nd, Gd, Dy, Y and Tm = Fe, Cr). It is expected that *Re*-site cation affects the symmetry of crystal structure due to large ionic radius and coordination number

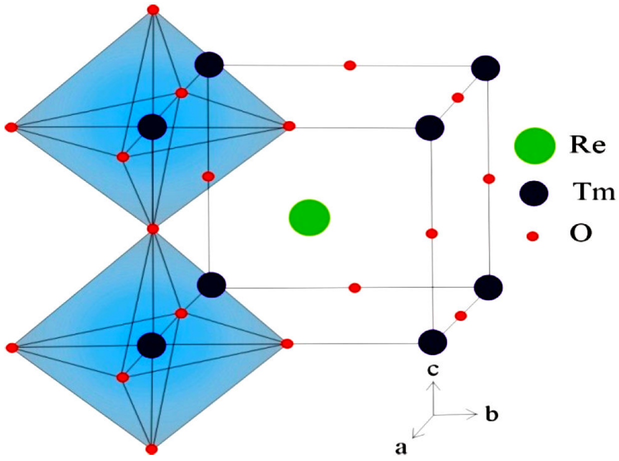

FIGURE 1. Orthorhombic perovskite structure of $ReTm\mathrm{O}_3$.

and Tm-site affect the octahedral distortion. Generally, the crystal symmetry of $ReTm\mathrm{O}_3$ can be controlled by variation of *Re* and *Tm* cations, giving the materials with some promising physical properties.

2. Experiment

$ReTm\mathrm{O}_3$ (Re = La, Nd, Gd, Dy, Y and Tm = Fe, Cr) were synthesized by using sol-gel method. In synthesis process, 100 ml of one mole rare earth nitrate hexahydrate $Re(\mathrm{NO}_3)_3.6\mathrm{H}_2\mathrm{O}$ (where *Re* = La, Ce, Nd, Gd, Dy, Y) solution was added to 100 ml of one mole transition metal nitrate nonahydrate $Tm(\mathrm{NO}_3)_3.9\mathrm{H}_2\mathrm{O}$ (*Tm* = Fe, Cr). One mole monohydrate citric acid $\mathrm{C}_6\mathrm{H}_8\mathrm{O}_7.\mathrm{H}_2\mathrm{O}$ in 100 ml deionized water was also mixed in above raw materials as a fuel or chelating agent. Metal nitrates to citrate ratio were kept at 1.5:1. The solution pH was set at 7 by adding proper amount of solution of ammonia ($\mathrm{NH}_4\mathrm{OH}$) (85% deionized water and 15% ammonia) drop wise during stirring process. The resulting aqueous solution was continuously stirred and heated at constant temperature of about 80°C, till viscous gel was formed after 2 hours. Afterwards, the gel was kept at a temperature of about 200°C. Later on, the gel started burning in a self propagated combustion manner, and voluminous porous powder were obtained. Finally, the fine powders of $Re\mathrm{FeO}_3$ and $Re\mathrm{CrO}_3$ were obtained and sintered at 800°C and 1000°C respectively for 3 h in a box furnace. Normal atmospheric conditions were used for synthesis and sintering process. The atmospheric pressure was used during sintering process in the environment of air. The resultant samples were obtained, the chemical equation explains the whole process,

$$\begin{aligned}\mathrm{Re(NO_3)_3.6H_2O} + \mathrm{Tm(NO_3)_3.9H_2O} + \mathrm{C_6H_8O_7.H_2O}\\ + \mathrm{NH_4OH} \rightarrow ReTm\mathrm{O}_3 + 6\mathrm{CO}_2\\ + 3.5\mathrm{N}_2(g) + n\mathrm{H}_2\mathrm{O}(g)\end{aligned} \tag{1}$$

where (*Re* = La, Ce, Nd, Gd, Dy, Y) and (*Tm* = Fe, Cr). Nucleation is responsible for the formation of grains. In our case transition metal ions act as seed crystal and responsible of nucleation during the sol-gel process. The stoichiometric ratio of rare earth and transition metal ions is equal, so more nucleation was observed in synthesis process that is responsible to nanocrystals formation. The phase identification was carried out using Bruker D8 advance X-ray diffractometer equipped with Cu-Kα source of X-rays of wavelength 1.54056 Å. Average grain size was estimated by Scherrer's formula considering the position and broadening of the most intense diffraction peak in XRD spectra and by Williamson Hall analysis. Morphology and elemental composition of the samples were observed using FEI NOVA 450 scanning electron microscope (SEM) equipped with Oxford energy dispersive X-rays spectroscopy (EDS) detector. The UV-visible measurements were taken by using Perkin Elmer Lambda 950 UV/VIS/NIR spectrophotometer.

3. Results and discussion

3.1. Structural and morphological Properties

Figure 2 shows the X-ray diffraction pattern of a representative sample LaFeO_3 among the prepared samples analyzed

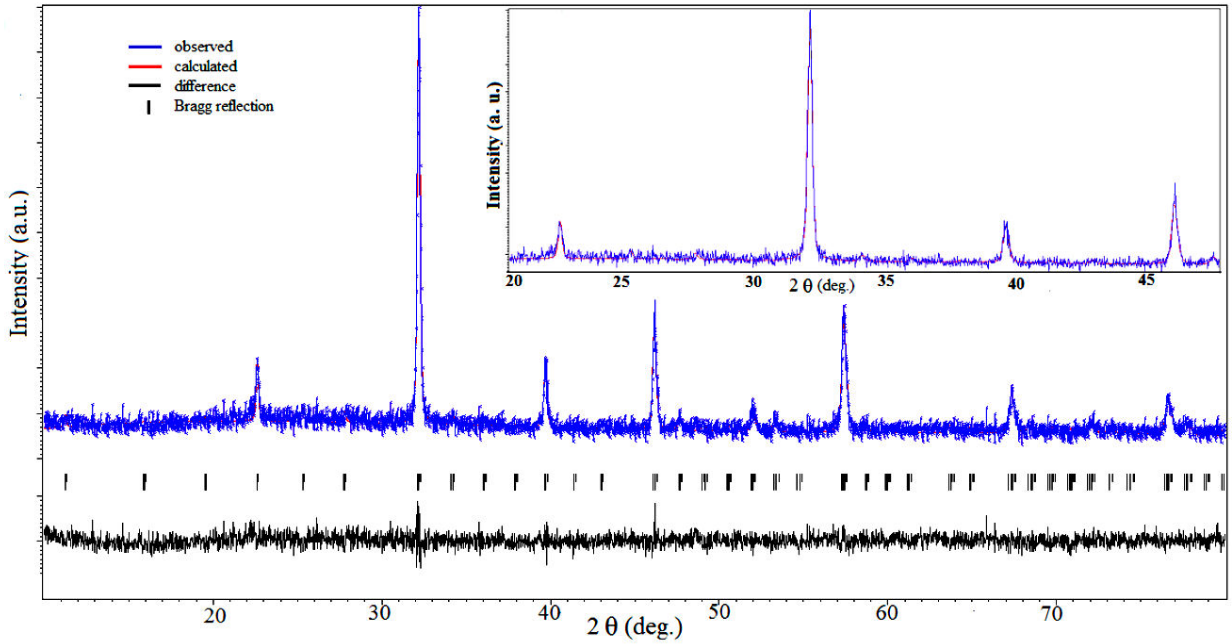

FIGURE 2. (color online) Rietveld refinement of the XRD pattern by using the JANA2006 program of representative sample LaFeO_3. Inset shows zoom region of the fit of calculated curve on observed curve.

TABLE I. Summary of XRD refined data of $ReTm\mathrm{O}_3$ (Re = La, Nd, Gd, Dy, Y and Tm = Fe, Cr). Where S.C (Sample Code), C.F (Chemical Formula), F.W (Formula Weight), C.S (Crystal Structure), S.G (Space Group), D.C (Data Collected).

S.C	LF(C)O	NF(C)O	GF(C)O	DF(C)O	YF(C)O
C.F	LaFe(Cr)O_3	NdFe(Cr)O_3	GdFe(Cr)O_3	DyFe(Cr)O_3	YFe(Cr)O_3
a (Å)	5.55 (5.48)	5.45 (5.42)	5.35 (5.31)	5.30 (5.262)	5.28 (5.24)
b (Å)	5.56 (5.51)	5.58 (5.48)	5.62 (5.52)	5.60 (5.50)	5.59 (5.51)
c (Å)	7.87 (7.76)	7.77 (7.69)	7.67 (7.60)	7.62 (7.55)	7.60 (7.53)
V (Å^3)	243.0 (234.3)	236.5 (228.6)	230.2 (222.6)	226.3 (262.5)	224.8 (217.4)
F.W	242.7 (238.9)	248.1 (244.2)	261.1 (257.2)	266.3 (262.5)	192.7 (188.9)
Z	4	4	4	4	4
C.S	Orthorhombic	Orthorhombic	Orthorhombic	Orthorhombic	Orthorhombic
S.G	Pbnm	Pbnm	Pbnm	Pbnm	Pbnm
S.G No.	62	62	62	62	62
D.C	$0 \leq h \leq 4$	$0 \leq h \leq 4$	$0 \leq h \leq 4$	$0 \leq h \leq 4$	$0 \leq h \leq 4$
	$0 \leq k \leq 4$	$0 \leq k \leq 5(4)$	$0 \leq k \leq 5(4)$	$0 \leq k \leq 5(4)$	$0 \leq k \leq 5(4)$
	$0 \leq l \leq 6$	$0 \leq l \leq 6$	$0 \leq l \leq 6$	$0 \leq l \leq 6$	$0 \leq l \leq 6$

by using Rietveld refinement technique considering orthorhombic structure with *Pbnm* space group. The pseudo-Voigt function was used to perform fitting of diffraction peaks by using the JANA2006 software. A good fitting has been clearly seen between observed and refined XRD data, as all the peaks are well overlapped with fitted data, which confirm single phase has been successfully formed and no impurity peak has been observed. All samples of $ReTm\mathrm{O}_3$ (Re = La, Nd, Gd, Dy, Y and Tm = Fe, Cr) were fitted by JANA2006 (not shown here). Figure 3(a) shows the XRD spectra of polycrystalline $ReTm\mathrm{O}_3$. The diffraction peaks are narrow and sharp, which reflects the high crystalline nature of the prepared samples. The diffraction pattern of $ReTm\mathrm{O}_3$ (Re = La, Nd, Gd, Dy, Y and Tm = Fe, Cr), suggest orthorhombic perovskite structure with space group *pbnm* (No. 62). The XRD pattern of polycrystalline Ce(Fe,Cr)O_3, where a couple of secondary phases are present as shown in Fig. 3(b). Thus single phase Ce(Fe,Cr)O_3 could not be obtained by sol-gel combustion method. The calculated lattice parameters (a, b, c), unit cell volume (V), and data collected about miller indices (hkl) of lattice planes of as prepared $ReTm\mathrm{O}_3$ (Re = La, Nd, Gd, Dy, Y and Tm = Fe, Cr), are tabulated in Table I. It is clearly shown that, in all cases, $c/\sqrt{2}$ lies between *a* and *b* ($b > c/\sqrt{2} > a$) (see Table I), this is the characteristic of the O-type orthorhombicaly distorted perovskite oxides [25], where the distortion occurs due to the steric effect and Jahn Teller effect [9].

The values of average grain size of $ReTm\mathrm{O}_3$, which was calculated by using the well known Scherrer's formula [$D = 0.89\lambda/\beta\cos\theta$, where λ is the wavelength of X-ray radiation (1.54056 Å), θ is the diffraction angle and β is the full width at half maximum (FWHM) of diffracted peaks], are shown in Table II and Table III. It is obvious to identify that the grain size decreases as ionic radius of *Re* and *Tm* decreases.

In nanomaterials lattice strain and grain size both have their self contribution to peak broadening of X-ray diffraction and lattice strain is to be contributed in peak broadening due to large volume of grain boundaries [26, 27]. In order to measure the grain size precisely, the lattice strain calculations are very important [28]. Hence, the Williamson-Hall (W-H) method was used for estimating the lattice strain and grain size [29, 30]. In addition, lattice strain and grain size independently contribute to the total peak broadening. The peak broadening induced by strain (β_S) is given by the relation $\beta_S = 4\varepsilon\tan\theta_{hkl}$. Assuming that the strain present in the material is uniform, the W-H equation for the total peak broadening is given by [31],

$$\beta_{hkl} = \beta_S + \beta_D, \tag{2}$$

$$\beta_{hkl} = 4\varepsilon\tan\theta_{hkl} + \left(\frac{k\lambda}{Dcos\theta_{hkl}}\right), \tag{3}$$

Rearranging Eq. (3) gives:

$$\beta_{hkl}\cos\theta_{hkl} = 4\varepsilon\sin\theta_{hkl} + \left(\frac{k\lambda}{D}\right), \tag{4}$$

where k is the shape factor and D is the grain size. A graph is plotted by taking $4\sin\theta_{hkl}$ along X-axis and $\beta\cos\theta_{hkl}$ along Y-axis as shown in Fig. 4. In W-H analysis, the strain present in the material is extracted from the slope and the grain size is estimated from the Y-intercept of the linear fit made to the plot. The estimated values of grain size and lattice strain are (60.52 nm) and (1.32×10^{-3}) for NdFeO_3 and (67.60 nm) and (2.57×10^{-3}) for NdCrO_3 respectively. The small values of lattice strain indicate that the volume of grain boundries should be small for prepared samples. The values of grain

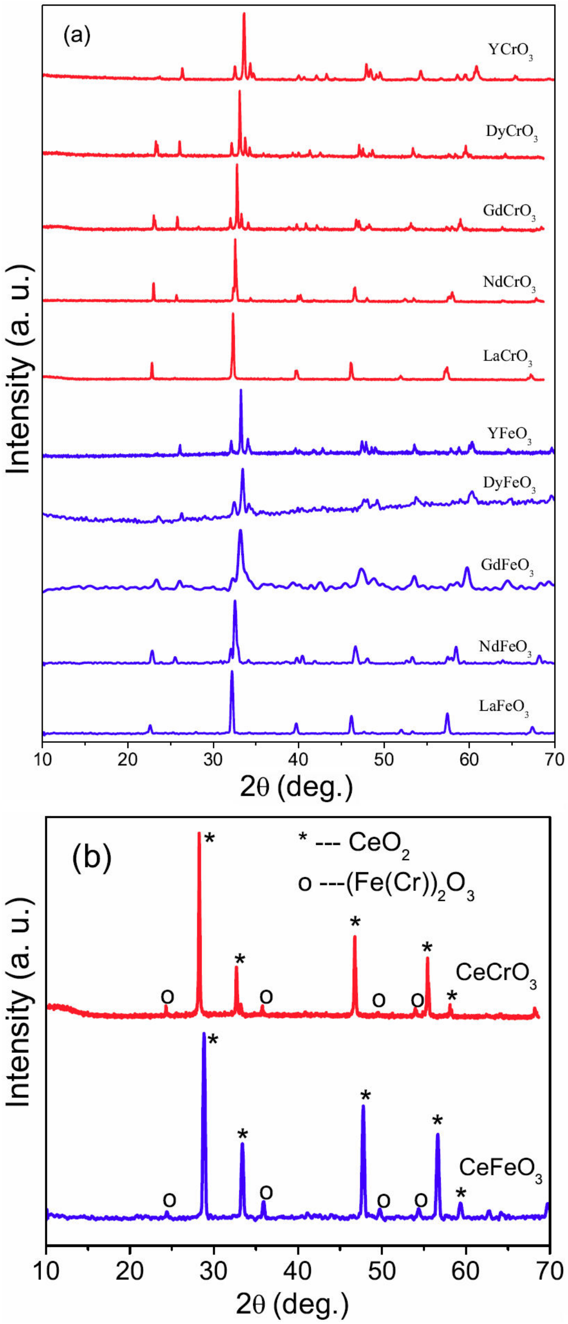

FIGURE 3. XRD pattern of (a) $ReTm\text{O}_3$ (Re = La, Nd, Gd, Dy, Y and Tm = Fe, Cr) and (b) Ce(Fe,Cr)O_3. The asterisks on the peaks show the cerium dioxide (CeO_2) phase and circles on the peaks show. Iron(III) oxide or ferric oxide (Fe_2O_3) and Chromium(III) oxide (Cr_2O_3).

size estimated by W-H analysis for ReFeO$_3$ and ReCrO$_3$ are shown in Table II and Table III, respectively. The SEM micrographs of all samples of the polycrystalline $ReTm\text{O}_3$ (Re = La, Nd, Gd, Dy, Y and Tm = Fe, Cr) which were taken at accelerating voltage of 10 KV and magnification of 80 K are shown in Fig. 5(a) to (l). Large grains with less grain boundaries can easily be seen from micrographs. However, grains show no perfect alignment, which is a typical characteristic of polycrystalline sample. The individual grains shown in the Fig. 5(a) to (l), are of the round shape with an average grain size 25-75 nm, which is consistent with XRD results. Moreover, from Fig. 5(f) and 5(l), which show the SEM images of $CeCrO_3$ and $CeFeO_3$ respectively, it is clear there is no formation of grains were observed as in other SEM images. These results also consistant with XRD analysis, the two phase formation in $CeCeO_3$ and $CeFeO_3$. In Fig. 6(a) to (l), EDX spectra show the chemical composition of the synthesized samples of $ReTm\text{O}_3$ (Re = La, Nd, Gd, Dy, Y and Tm = Fe, Cr). It can be seen that there are clear peaks of rare earth elements (Re = La, Nd, Gd, Dy, Y), Iron (Fe), Chromium (Cr), and oxygen (O) elements present with the molar ratio of about 1:1:3 (Re:Fe(Cr):O), giving a stoichiometric formula for ReFe(Cr)O_3, confirmed with analysis of atomic % of all elements present in a sample shown in Fig. 6(a) to (l). There is no peak of any impurity elements which confirms the single phase formation of the samples. However, single peak of carbon appeared which is due to the carbon tape on which samples were mounted with holder. The value of average grain size calculated from XRD pattern is consistent with the one obtained from SEM analysis.

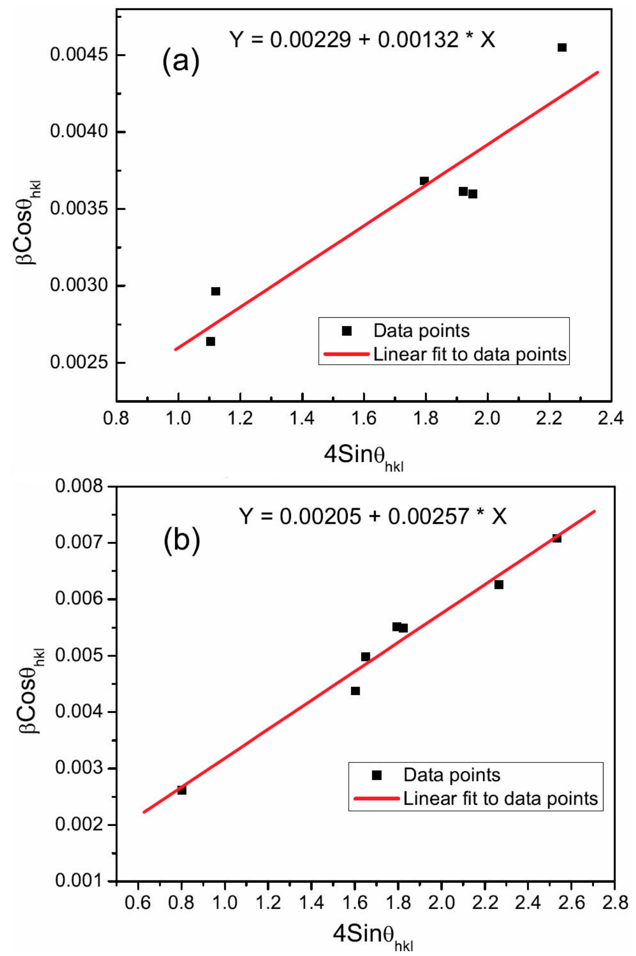

FIGURE 4. Williamson Hall analysis of (a) $NdFeO_3$ and (b) $NdCrO_3$.

The variation in lattice parameters ($a, b, c/\sqrt{2}$) and cell volume (V) with ionic radii of rare earth cations on *Re* site in

TABLE II. Crystallographic characteristics of $Re\mathrm{FeO}_3$ (*Re* = La, Nd, Gd, Dy, Y).

Sample Code Chemical formula	LFO $LaFeO_3$	NFO $NdFeO_3$	GFO $GdFeO_3$	DFO $DyFeO_3$	YFO $YFeO_3$
Orthorhombic distortion (D)	0.4150	0.4102	0.4056	0.4057	0.4056
Cell distortion (d) $\times 10^{-6}$	3	386	1673	2005	2252
Orthorhombic strain (S)	0.0018	0.0237	0.0493	0.0543	0.0577
Elastic strain (E)	0.0552	0.0600	0.0656	0.0693	0.0723
Grain size (nm)(Scherrer formula)	52.38	39.00	31.62	27.78	25.48
Grain size (nm)(W-H analysis)	67.56	60.52	47.38	40.29	35.77
BET surface area (m^2/g)	17.26	22.08	25.18	27.61	41.32
X-ray density (d_{x-ray}) (g/cm^3)	6.64	6.97	7.54	7.82	5.70
Bulk density (d_{bulk}) (g/cm^3)	5.20	5.43	5.92	6.11	3.32
Porosity(P)	0.2163	0.2212	0.2147	0.2193	0.4178

TABLE III. Crystallographic characteristics of $Re\mathrm{CrO}_3$ (*Re* = La, Nd, Gd, Dy, Y).

Sample Code Chemical formula	LCO $LaCrO_3$	NCO $NdCrO_3$	GCO $GdCrO_3$	DCO $DyCrO_3$	YCO $YCrO_3$
Orthorhombic distortion (D)	0.0047	0.0071	0.0272	0.0323	0.0358
Cell distortion (d) $\times 10^{-6}$	30	60	940	1320	1620
Orthorhombic strain (S)	0.0062	0.0097	0.0375	0.0446	0.0493
Elastic strain (E)	0.0599	0.0653	0.0708	0.0749	0.0766
Grain size (nm)(Scherrer formula)	55.00	41.62	38.82	36.89	33.79
Grain size (nm)(W-H analysis)	72.30	67.60	53.52	44.29	41.47
BET surface area (m^2/g)	16.05	20.32	20.14	20.38	30.77
X-ray density (d_{x-ray}) (g/cm^3)	6.78	7.09	7.68	7.98	5.77
Bulk density (d_{bulk}) (g/cm^3)	5.05	5.28	5.77	5.96	3.17
Porosity(P)	0.2545	0.2565	0.2488	0.2537	0.4514

the prepared $Re\mathrm{FeO}_3$ (*Re* = La, Nd, Gd, Dy, Y) is shown in Fig. 7(a). It is obvious from the graph that *a*, $c/\sqrt{2}$ and *V* increases with the increase in the ionic radius of *Re* site ion *i.e.* [from Y^{3+} (1.04 Å) to La^{3+} (1.172 Å)], but lattice parameter b remains almost unaltered. The similar variations were observed in lattice parameters and cell volume for $Re\mathrm{CrO}_3$ (*Re* = La, Nd, Gd, Dy, Y), not shown in the graph, but values for this system are given in Table I.

The orthorhombic factor (b/a) sharply increases, with decreasing ionic radius of *Re* site in $Re\mathrm{FeO}_3$, as shown in the Fig. 7(b). Similar trend is also obtained for $Re\mathrm{CrO}_3$, not shown here. To study the structural distortion, cell distortion (d) [32] was calculated as,

$$d=\frac{\left[(a/\sqrt{2}-a_p)^2+(b/\sqrt{2}-a_p)^2+(c/2-a_p)^2\right]}{3a_p}\times 10^4, \quad (5)$$

where $a_p = (a/\sqrt{2}+b/\sqrt{2}+c/2)/3$. The value of cell distortion increases for both $Re\mathrm{Fe(Cr)O}_3$ by the replacement of large ionic radius La^{3+} to small ionic radius Y^{3+} are given in Table II and Table III. It is worth mentioning that the decrease in cell distortion has been observed when we replace bigger Re^{3+} cation in $Re\mathrm{FeO}_3$ as indicated in Fig. 7(c), similar results were obtained for $Re\mathrm{CrO}_3$. According to the analysis mentioned above, the variance of lattice parameters with coupled substitution on *Re* site and on *Tm* site is the result of distortion in $Tm\mathrm{O}_6$ octahedra for matching *Re* sizes. That is why distortion at octahedral site increases with replacement of the small ionic radius on *Re* site, because the cations rearrange themselves in such a way that they fit in the unit cell and results in decreasing the unit cell volume.

Orthorhombic distortion (D), which is defined as the ratio of standard deviation to average of the lattice parameters is calculated as [33],

$$D=\frac{\sqrt{\sum(a_i-\bar{a})^2}}{\bar{a}}, \quad (6)$$

where a_i = *a*, *b* and $c/\sqrt{2}$ and $\bar{a}$ is the average of a_i. The orthorhombic distortion remains almost constant in region of ionic radii of $Re^{3+} \leq 1.078$ Å, in this region lattice parameter *b* increases slightly. After further increase in ionic radii

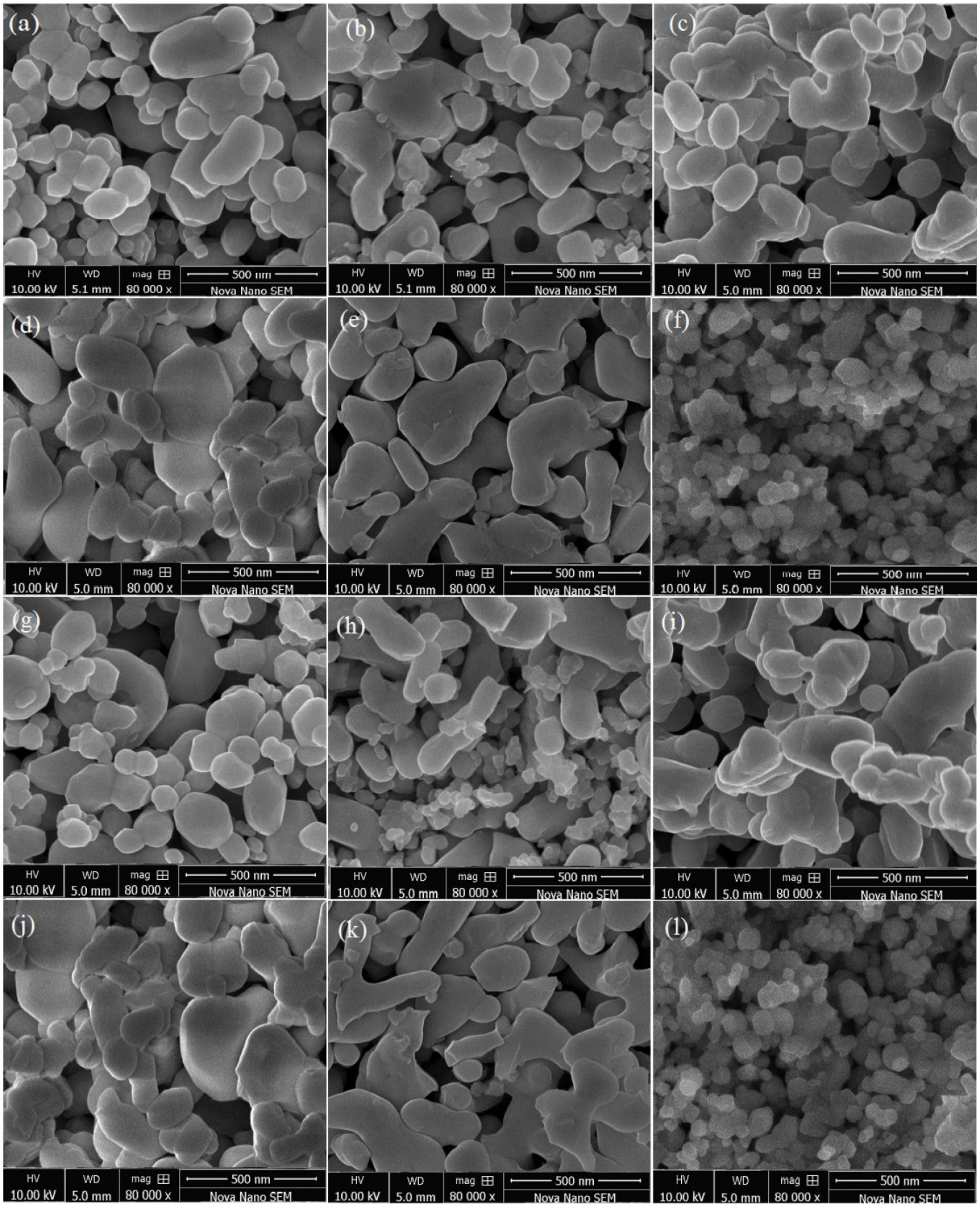

FIGURE 5. SEM images of perovskite (a) $LaCrO_3$ (b) $NdCrO_3$ (c) $GdCrO_3$ (d) $DyCrO_3$ (e) $YCrO_3$ (f) $CeCrO_3$ (g) $LaFeO_3$ (h) $NdFeO_3$ (i) $GdFeO_3$ (j) $DyFeO_3$ (k) $YFeO_3$ and (l) $CeFeO_3$.

of Re^{3+} a linear increase has been observed in orthorhombic distortion, in this region lattice parameter *b* slightly decreases. The variation in orthorhombic distortion with Re^{3+} ionic radii is shown in Fig. 7(c). The elastic strain of the prepared compounds can be calculated by using the formula E = $\beta/2\cot\theta$ [34]. The value of elastic strain increases with the decrease in the grain size both for $Re\mathrm{FeO}_3$ and $Re\mathrm{CrO}_3$ as obvious from Table II and Table III. The observed variation in the calculated elastic strain in $Re\mathrm{Fe(Cr)O}_3$ elaborate the broadening of the XRD pattern. The elastic strain decreases with the increase in *Re* site ionic radii for $Re\mathrm{FeO}_3$ as shown in Fig. 7(d). The spontaneous orthorhombic strain, defined as

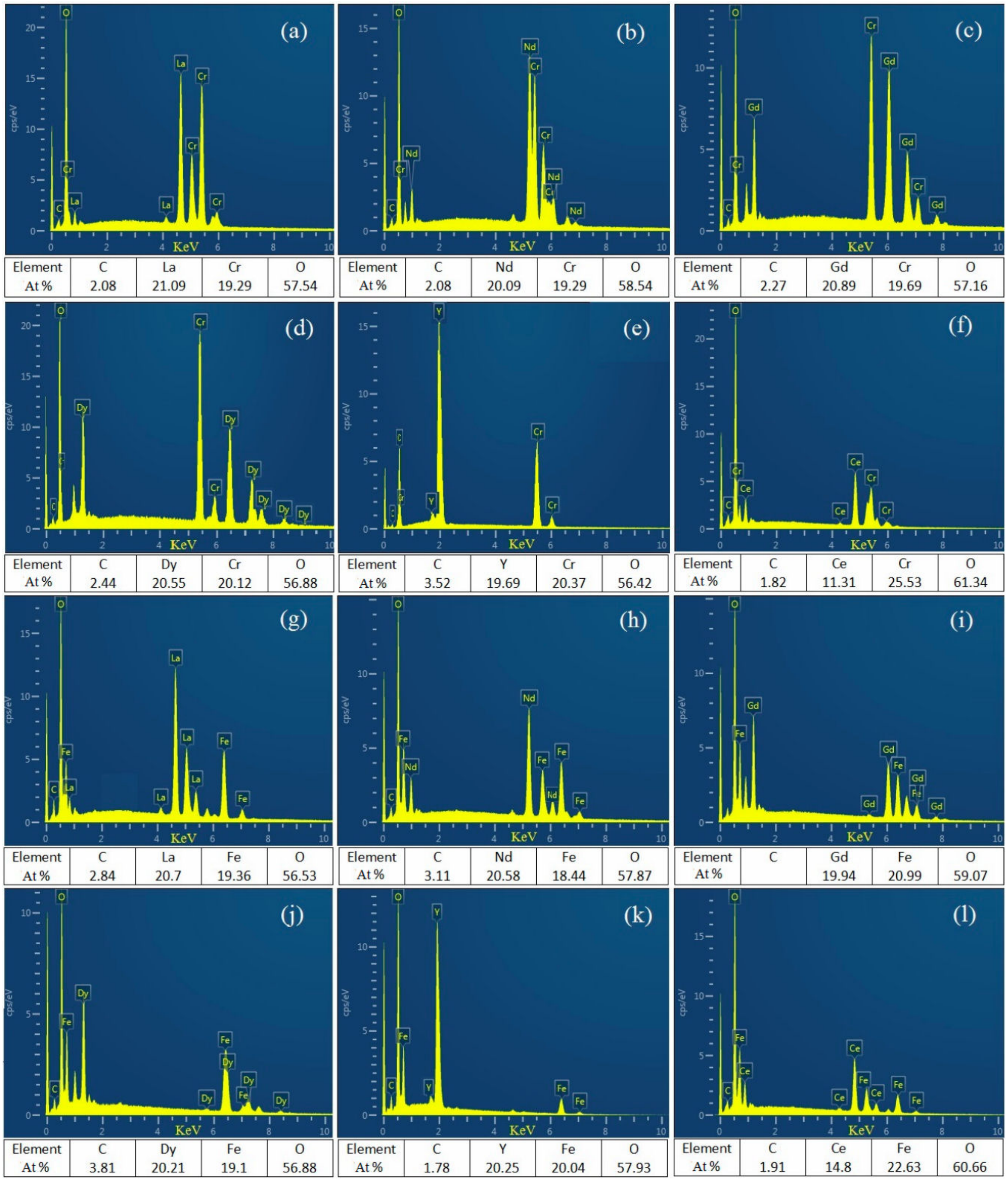

(a)

Element	C	La	Cr	O
At %	2.08	21.09	19.29	57.54

(b)

Element	C	Nd	Cr	O
At %	2.08	20.09	19.29	58.54

(c)

Element	C	Gd	Cr	O
At %	2.27	20.89	19.69	57.16

(d)

Element	C	Dy	Cr	O
At %	2.44	20.55	20.12	56.88

(e)

Element	C	Y	Cr	O
At %	3.52	19.69	20.37	56.42

(f)

Element	C	Ce	Cr	O
At %	1.82	11.31	25.53	61.34

(g)

Element	C	La	Fe	O
At %	2.84	20.7	19.36	56.53

(h)

Element	C	Nd	Fe	O
At %	3.11	20.58	18.44	57.87

(i)

Element	C	Gd	Fe	O
At %		19.94	20.99	59.07

(j)

Element	C	Dy	Fe	O
At %	3.81	20.21	19.1	56.88

(k)

Element	C	Y	Fe	O
At %	1.78	20.25	20.04	57.93

(l)

Element	C	Ce	Fe	O
At %	1.91	14.8	22.63	60.66

FIGURE 6. EDX images of perovskite (a) $LaCrO_3$ (b) $NdCrO_3$ (c) $GdCrO_3$ (d) $DyCrO_3$ (e) $YCrO_3$ (f) $CeCrO_3$ (g) $LaFeO_3$ (h) $NdFeO_3$ (i) $GdFeO_3$ (j) $DyFeO_3$ (k) $YFeO_3$ and (l) $CeFeO_3$.

S = 2(a - b)/(a + b), is tabulated in Table II. The value of S decreases from 0.0577 to 0.0118 for YFO to LFO. The variation in orthorhombic strain with ionic radius of rare earth cations is shown in Fig. 7(d). The reason for decrease of this parameter may be the substitution on *Re* site of smaller ionic radius cation Y^{3+} to bigger La^{3+}. The similar results also obtained for YCO to LCO *i.e.* 0.0493 to 0.0062. It is obvious from the results that replacement of small radius transition metal cation Fe^{3+} to big radius Cr^{3+} on *Tm*-site of $ReTm\mathrm{O}_3$ also gives the similar trend *i.e.* decrease in the orthorhombic strain. The X-ray density, bulk density and porosity for all samples were determined using the following relations [35]

$$d_{x-ray} = \frac{ZM}{N_A V_{cell}}, \tag{7}$$

where M the molar mass, Z is the number of molecules per formula unit (4 for the orthorhombic structure), N_A Avogadro s number (6.02×10^{23} /mole) and V_{cell} is the unit cell

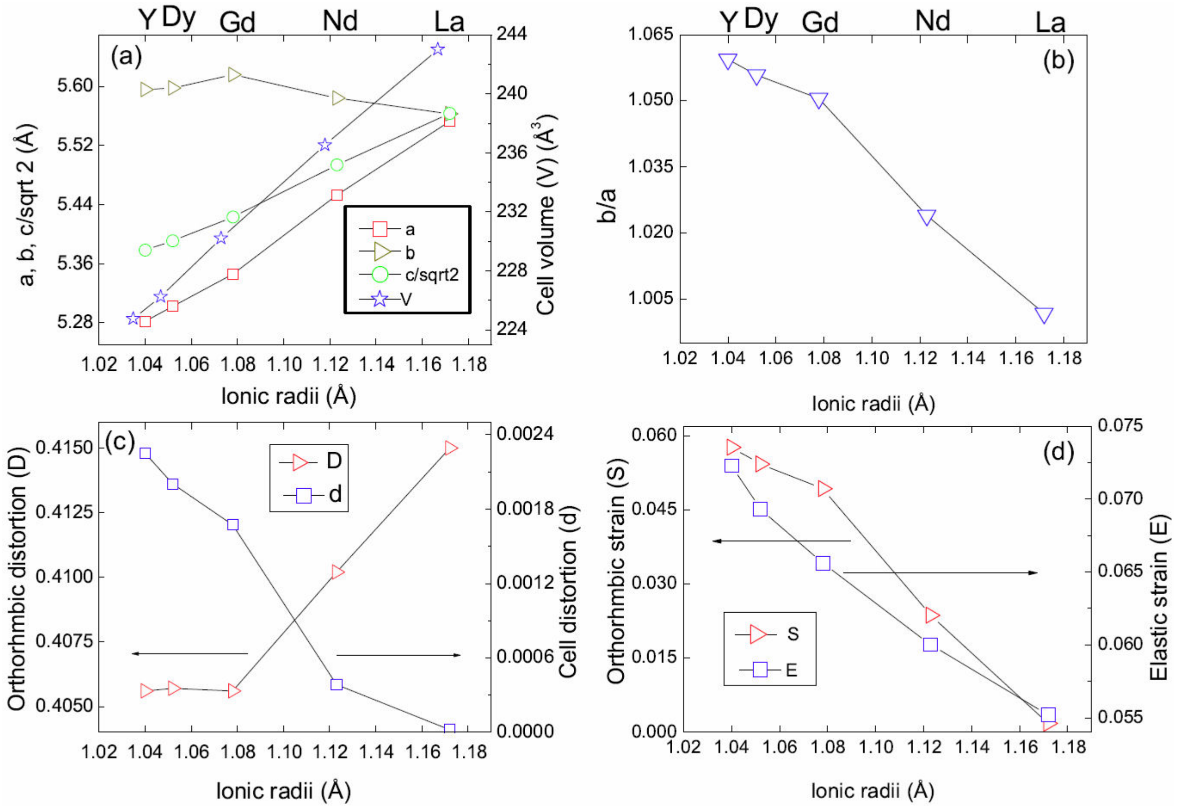

FIGURE 7. Variation of (a) lattice parameters $(a, b, c/\sqrt{2})$ and cell volume V. (b) Orthorhombicity factor (b/a). (c) Orthorhombic distortion (D) and cell distortion (d). (d) Orthorhombic strain (S) and Elastic strain (E) with ionic radius of *Re*-site.

volume. The bulk density was calculated by the following relation,

$$d_{bulk} = \frac{m}{V}, \tag{8}$$

where m is the mass and $V = \pi r^2 h$ (where r is the radius and h is the height/thickness of pellet) is the volume of the pellet. The porosity (P) of all the samples was calculated using the equation,

$$P = 1 - \frac{d_b}{d_x}, \tag{9}$$

where d_b is the bulk density and d_x is the X-ray density. The measured values of d_x, d_b, and P of ReFeO$_3$ for various *Re* (Re = La, Nd, Gd, Dy, Y) site replacement are tabulated in Table II. Figure 8 shows that the d_x and the d_b increase with increase in the formula weight of the prepared ReFeO$_3$ for various *Re* (Re = La, Nd, Gd, Dy, Y) compounds. The increase in the d_x is considered to be due to the fact that the atomic mass of various *Re* [Re= Y (89 amu), La (139 amu), Nd (144 amu), Gd (157 amu), Dy (162.5 amu)] increases due to which formula weight or mass of the compound increases [36]. While the increase in the d_b is due to the fact that increase in value of densities of *Re* [Re = Y (4.472 g/cm^3), La (6.162 g/cm^3), Nd (7.400 g/cm^3), Gd (7.900 g/cm^3), Dy (8.536 g/cm^3)]. The magnitude of the d_b is smaller than that of the d_x as can be seen from the graph. These results indicate that the experimental d_b is less than the theoretical d_x due to the presence of pores created during preparation or sintering process of the samples [37]. Figure 8 shows the P decreases with the increase of formula weight of the sample from YFO to LFO, but remains almost constant for further increase in the formula weight of prepared compounds. The increase in the d_b confirms that samples become denser with the increase in density of individual *Re* site element, due to which the porosity of the samples decreases.

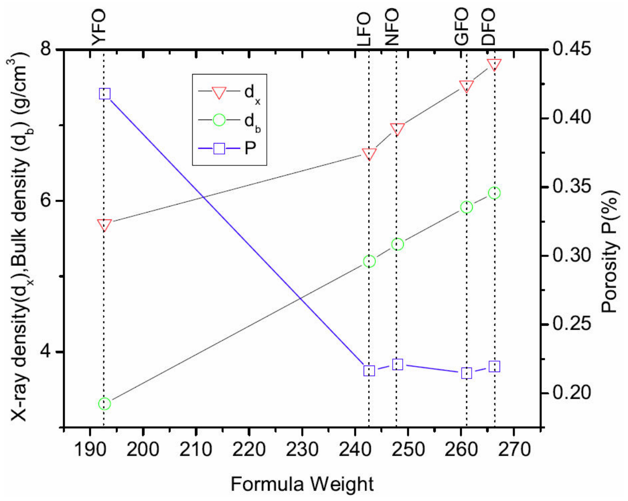

FIGURE 8. Variation in x-ray density (d_x), bulk density (d_b) and porosity (P) with variation of the formula weight of ReFeO$_3$ (Re = Y, La, Nd, Gd, Dy).

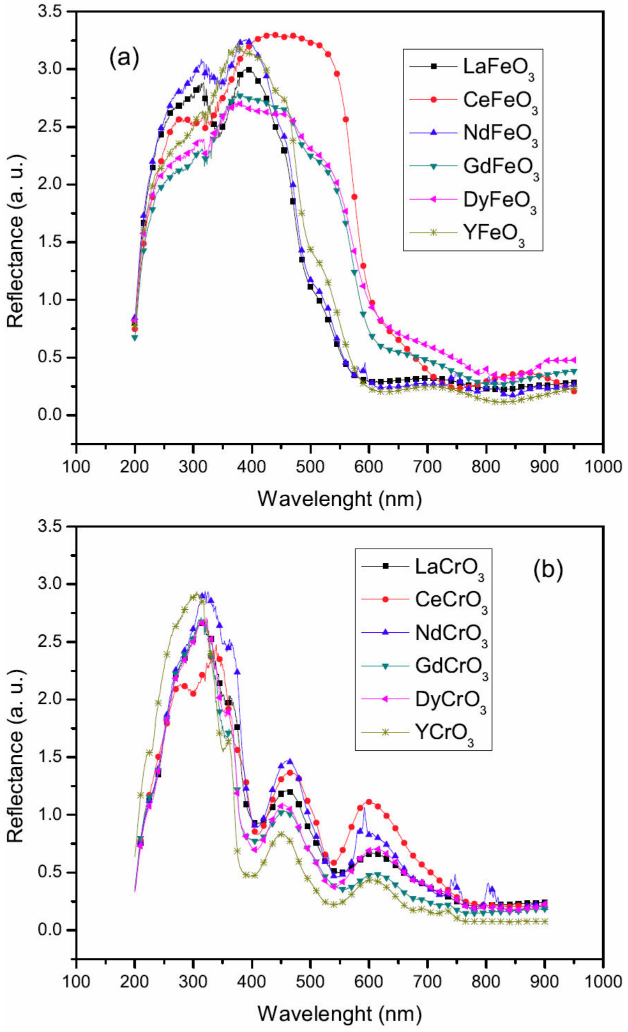

FIGURE 9. UV-visible reflectance spectra of (a) ReFeO$_3$ and (b) ReCrO$_3$.

The Brunauer-Emmett-Teller (BET) specific surface areas of $ReTm$O$_3$ (Re = La, Nd, Gd, Dy, Y and Tm = Fe, Cr) nanoparticles are measured by the BET relation of the form,

$$BET = \frac{6}{(d_{x-ray})D}, \tag{10}$$

where D is the orthorhombic distortion and d_{x-ray} is the X-ray density. The values of the specific surface area are given in Table II and III for ReFeO$_3$ and ReCrO$_3$, respectively.

3.2. Optical Properties

The obtained UV-visible diffuse reflectance spectra (DRS) of ReFeO$_3$ and ReCrO$_3$ (Re = La, Ce, Nd, Gd, Dy, Y) were measured by using UV/VIS/NIR spectrophotometer and are shown in Fig. 9(a) and (b), respectively. The absorbance spectrum of ReFeO$_3$ and ReCrO$_3$ is obtained from their reflectance spectrum according to the Kubelka-Munk theory [38]. Moreover, optical energy band gap of ReFeO$_3$ and ReCrO$_3$ (Re = La, Ce, Nd, Gd, Dy, Y) is estimated by using the Tauc relation [39].

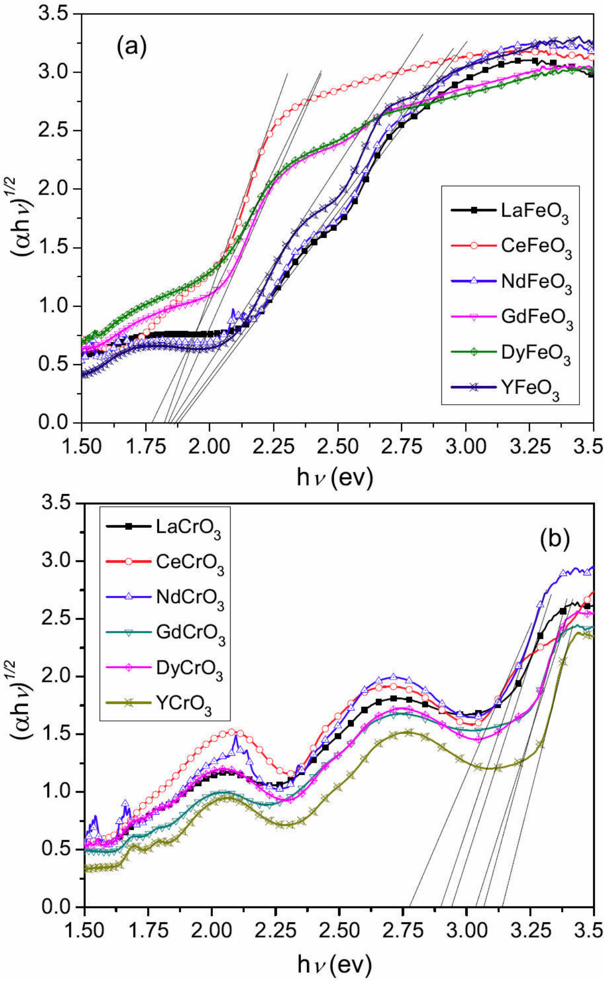

FIGURE 10. Tauc plot of (a) ReFeO$_3$ and (b) ReCrO$_3$.

$$\alpha h\nu = A(h\nu - E_g)^n, \tag{11}$$

where hv is the energy of the incident photon, α is the absorption coefficient, A is a characteristic parameter, E_g is the band gap. Exponent n specify the type of transition and it may be 1/2 or 2 for the allowed direct or allowed indirect transition, respectively. Here, we assume a direct band gap system and from the plot of $(\alpha h\nu)^{1/2}$ versus $h\nu$ by extrapolating the linear portion to the $h\nu$ (*i.e.* α = 0) determine the E_g. The obtained value of E_g for ReFeO$_3$ and ReCrO$_3$ is found to be in the range 1.77 - 1.87 eV and 2.77 - 3.14 eV, respectively as shown in Fig. 10(a) and (b). It is noted that in ReFeO$_3$ only single band gap is observed due to the transition from O 2p valence band to Fe 3d conduction band. This constitues a charge transfer energy gap. Interestingly, three edges are observed for ReCrO$_3$ at 1.58 eV, 2.20 eV and 3.14 eV values for YCrO$_3$. Khuong P Ong *et al*. have also observed three types of energy gap in LaCrO$_3$ theoretically [40]. Interestingly similar trend of energy gaps were also observed experimentally in our prepared compounds of family of orthochromites. The energy gap at 1.58 eV (value for YCrO$_3$), which is the energy band gap among the occupied t$_{2g}$ (Cr

$d_{x^2-y^2}$, d_{xz}, and d_{yz}) and unoccupied e_g (Cr d_{z^2} and d_{xy}) states, has been observed. This type of energy gap is Mott-type insulating gap. The second edge at 2.20 eV (value for YCrO$_3$) reveals the optical transitions between the Cr t_{2g} and Cr e_g bands which are, of course, partly hybridized with O p. These transitions are in visible range and indicate the color of various orthocromites ReCrO$_3$. The theoretical calculation reveals that the green color of these prepared compounds have its origin from the transition between Cr t_{2g} bands centered at (-0.23 eV) and Cr e_g bands at (2.15 eV) [40]. Another important transition at 3.14 ev (value for YCrO$_3$), shows the transition between the top of O p bands and the bottom of the Cr e_g conduction bands, this constitues a charge transfer gap. T. Arima *et al*. estimated E_g for LaCrO$_3$ and YCrO$_3$ experimentally [41,42], which is consistent with the observed values of optical band gap of ReCrO$_3$. So far, the experimental optical gap at higher energy edge for ReCrO$_3$ was considered as the energy band gap between the transition to the top of the valance band and the bottom of the conduction band by previous theoretical works [43–45]. The minimum E_g for Fe-based system (*i.e.* 1.77 eV) than that of Cr-based system (*i.e.* 2.77 eV) may be attributed to lower energy of 3d orbital of Fe than that of Cr.

4. Conclusion

The sol-gel auto combustion citrate method is successfully used for the synthesis of polycrystalline $ReTm$O$_3$ (Re = La, Nd, Gd, Dy, Y and Tm = Fe, Cr) and single phase character has been confirmed by XRD patterns. A systematic increase in grain size with increasing r$_{Re}$ and r$_{Tm}$ has been observed and found to vary from 25-75 nm for both ReFeO$_3$ and ReCrO$_3$, which is consistant with SEM results. The various crystallographic parameters have been calculated and found to be affected by changing *Re* and *Tm* sites as described earlier. The allowed direct E_g estimated to be 1.77 - 1.87 eV and 2.77 - 3.14 eV for ReFeO$_3$ and ReCrO$_3$, respectively. Three edges are observed for ReCrO$_3$ at 1.58 eV which is a Mott-type insulating gap, at 2.20 eV are in visible range corresponds to light green color of orthocromates and at 3.14 eV this is due to charge transfer gap (E_g) between O 2p valance and Cr 3d conduction band. Moreover, the E_g has larger value ($\sim$ 1 eV) in ReCrO$_3$ as compared to ReFeO$_3$ which may be attributed to the Jahn Teller distortion.

1. J.-S. Zhou, J. Goodenough, B. Dabrowski, *Phys. Rev. lett.* **95** (2005) 127204.
2. J. Torrance, P. Lacorre, A. Nazzal, E. Ansaldo, C. Niedermayer, *Phys. Rev. B* **45** (1992) 8209.
3. X. Granados, J. Fontcuberta, X. Obradors, L. Manosa, J. Torrance, *Phys. Rev. B* **48** (1993) 11666.
4. N. Q. Minh, *J. Am. Ceram. Soc.* **76** (1993) 563.
5. K. Haralambous, Z. Loizos, N. Spyrellis, *Mater. Lett.* **11** (1991) 133.
6. C. Alcock, R. Doshi, Y. Shen, *Solid State Ionics* **51** (1992) 281.
7. H. Aono, E. Traversa, M. Sakamoto, Y. Sadaoka, *Sens. Actuators, B* **94** (2003) 132.
8. S. Bukhari, J. Ahmad, *Acta Phys. Pol., A* **129** (2016) 43.
9. F.-K. Chiang, M.-W. Chu, F. Chou, H. Jeng, H. Sheu, F. Chen, C. Chen, *Phys. Rev. B* **83** (2011) 245105.
10. B. Naidu, U. Gupta, U. Maitra, C. Rao, *Chem. Phys. Lett.* **591** (2014) 277.
11. P. Negi, G. Dixit, H. Agrawal, R. Srivastava, *J. supercond. Novel* Magn. **26** (2013) 1611.
12. S. Saha, S. Chanda, A. Dutta, T. Sinha, *Mater. Res. Bull.* **48** (2013) 4917.
13. X. Wang, D. Li, T. Cui, P. Kharel, W. Liu, Z. Zhang, *J. Appl. Phys.* **107** (2010) 09B510.
14. O. Buassi-Monroy, C. Luhrs, A. Chávez-Chávez, C. Michel, *Mater. Lett.* **58** (2004) 716.
15. M. Alifanti, G. Bueno, V. Parvulescu, V. Parvulescu, V. C. Corberan, *Catal. Today* **143** (2009) 309.
16. W. Chen, F. Li, J. Yu, *Mater. Lett.* **61** (2007) 397.
17. V. Dudnikov, D. Velikanov, N. Kazak, C. Michel, J. Bartolome, A. Arauzo, S. Ovchinnikov, G. Patrin, *Phys. Solid State* **54** (2012) 79.
18. L. Predoana, B. Malic, M. Kosec, M. Carata, M. Caldararu, M. Zaharescu, *J. Eur. Ceram. Soc.* **27** (2007) 4407.
19. S. Saha, S. Chanda, A. Dutta, T. Sinha, *J. Sol-Gel Sci. Technol.* **69** (2014) 553.
20. S. Mathur, H. Shen, N. Lecerf, A. Kjekshus, H. Fjellvaag, G. F. Goya, *Adv. Mater.* **14** (2002) 1405.
21. A. Wu, H. Shen, J. Xu, L. Jiang, L. Luo, S. Yuan, S. Cao, H. Zhang, *J. Sol-Gel Sci. Technol.* **59** (2011) 158.
22. S. Hui, X. Jiayue, W. Anhua, *J. Rare Earth.* **28** (2010) 416.
23. S. Wang, K. Huang, C. Hou, L. Yuan, X. Wu, D. Lu, *Dalton Trans.* **44** (2015) 17201.
24. A. P. B. Selvadurai, V. Pazhanivelu, C. Jagadeeshwaran, R. Murugaraj, I. P. Muthuselvam, F. Chou, P. M. Gazzali, G. Chandrasekaran, *J. Sol-Gel Sci. Technol.* **80** (2016) 827.
25. E. Pollert, S. Krupička, E. Kuzmičová, *J. Phys. Chem. Solids* **43** (1982) 1137.
26. B. Hall, D. Zanchet, D. Ugarte, *J. Appl. Crystallogr.* **33** (2000) 1335.
27. H. Jiang, M. Rühle, E. Lavernia, *J. Mater. Res.* **14** (1999) 549.
28. V. Biju, N. Sugathan, V. Vrinda, S. Salini, *J. Mater. Sci.* **43** (2008) 1175.

29. G. Williamson, W. Hall, *Acta Metall.* **1** (1953) 22.
30. F. Mustafa, S. Aslam, A. Jamil, M. A. Ahmad, *Optik* **140** (2017) 38.
31. A. W. Burton, K. Ong, T. Rea, I. Y. Chan, *Microporous Mesoporous Mater.* **117** (2009) 75.
32. G. Huo, D. Song, Q. Yang, F. Dong, *Ceram. Int.* **34** (2008) 497.
33. K. Knížek, Z. Jirák, J. Hejtmánek, M. Veverka, M. Maryško, G. Maris, T. Palstra, *Eur. Phys. J. B* **47** (2005) 213.
34. R. Kelsall, I. W. Hamley, M. Geoghegan, *Nanoscale science and technology*, (John Wiley & Sons, 2005).
35. J. Ahmad, M. Q. Awan, M. E. Mazhar, M. N. Ashiq, *Physica B* **406** (2011) 254.
36. A. Sattar, *Egptian J Sol* **27** (2004) 99.
37. M. Ahmed, N. Okasha, M. Oaf, R. Kershi, *J. Magn. Magn. Mater.* **314** (2007) 128.
38. P. Kubelka, F. Munk, *Z. Tech. Phys* **12** (1931) 593.
39. J. Tauc, R. Grigorovici, A. Vancu, *Phys. Status Solidi B* **15** (1966) 627.
40. K. P. Ong, P. Blaha, P. Wu, *Phys. Rev. B* **77** (2008) 073102.
41. T. Arima, Y. Tokura, J. Torrance, *Phys. Rev. B* **48** (1993) 17006.
42. T.-h. Arima, Y. Tokura, *J. Phys. Soc. Jpn.* **64** (1995) 2488.
43. N. Hamada, H. Sawada, K. Terakura, *Spectroscopy of Mott Insulators and Correlated Metals* (1995) pp. 95–105.
44. I. Solovyev, N. Hamada, K. Terakura, *Phys. Rev. B* **53** (1996) 7158.
45. Z. Yang, Z. Huang, L. Ye, X. Xie, *Phys. Rev. B* **60** (1999) 15674.